International Journal of Impact Engineering 59 (2013) 46–59

Contents lists available at SciVerse ScienceDirect

International Journal of Impact Engineering

journal homepage: www.elsevier.com/locate/ijimpeng

Deformation and failure of rectangular plates subjected to impulsive loadings

Ye Yuan, P.J. Tan*

Department of Mechanical Engineering, University College London, Torrington Place, London WC1E 7JE, UK

ARTICLE INFO

Article history:
Received 25 July 2012
Received in revised form
15 January 2013
Accepted 21 March 2013
Available online 4 April 2013

Keywords:
Impulsive loads
Damage
Ductile fracture
Rectangular plates
Deformation maps

ABSTRACT

The deformation and failure of fully-clamped rectangular plates subjected to zero-period, *uniform-momentum* impulsive loads are studied. Analytical predictions are given for the critical velocities corresponding to the transition between deformation modes. Three-dimensional (3D) numerical analyses were performed using the non-linear finite element (FE) code ABAQUS/Explicit® to predict the maximum central deflection and deformation mode of rectangular plates for different combinations of aspect ratios and impulses. Two competing mechanisms of bulk material failure, viz. by the nucleation, coalescence and growth of voids and by shear band localisation, are implemented in the FE model to simulate tensile tearing, resulting in progressive ductile fracture, at the support. The numerical results are validated against experimental data for square mild-steel and aluminium plates where they are found to be in good agreement. Deformation maps delineating the different deformation régimes for different combinations of blast impulse and aspect ratio are constructed for plates of equal mass. The effects of imposing a finite-period, as opposed to a zero-period, impulsive load upon the deformation mode and maximum deflection are also discussed.

1. Introduction

The classical experiment of Menkes and Opat [1] showed that the mode of deformation in a fully-clamped monolithic beam subjected to impulsive loading is dependent upon the non-dimensional impulse I^* and is classified according to: mode I (large inelastic deformation), mode II (tensile-tearing and deformation) and mode III (shear-band localisation). Nurick and Shave [2] also observed the same for impulsively-loaded square plates. In addition, they proposed that the mode II deformation may be subdivided into three distinct régimes of *mode* II* (through-thickness tearing along the support), mode IIa (complete detachment from support with maximum central deflection *increasing* with I^*) and mode IIb (complete detachment from support with maximum central deflection *decreasing* with I^*). To the best of the authors' knowledge, nearly all the available experimental data in the literature [3–5], with the notable exception of [6], were for square plates. Hitherto, it remains unclear how aspect ratio γ affects the mode of deformation in rectangular plates where $\gamma > 1$. In a similar vein, little is known of how the fixing conditions at the support affect the tearing mechanism in the plate which, in turn, has an effect upon the plate performance. The aforementioned issues are addressed in this paper which will present the results of a detailed numerical study to elucidate how combinations of blast impulse and aspect ratio affect the deformation mode and how limits to deformation, caused by necking localisation and/or ductile fracture at the support, affect the overall performance of rectangular plates to impulsive loadings. The motivation of this work is to establish a protocol that would allow the effects of support conditions to be incorporated into the assessment metric when evaluating the blast performance of monolithic and sandwich plates; this is part of a wider study into the combined blast and impact loading of structures to be reported elsewhere.

The present study focuses on the response of rectangular monolithic plates to zero-period, *uniform-momentum* impulses. It is assumed that the loading is imparted by a blast pulse of a much shorter duration compared to the characteristic time needed for the plate to reach its maximum transverse displacement [7,8]. Critical impulses corresponding to the transition between deformation modes are derived analytically in Section 2. Three-dimensional FE simulations are carried out using ABAQUS/Explicit® to compute the plate resistance to impulsive blast loads. Only aluminium and mild-steel plates are considered in this study to allow validation with experimental data in existing literature

* Corresponding author. Tel.: +44 020 7679 3754; fax: +44 020 7388 0180.
E-mail address: pj.tan@ucl.ac.uk (P.J. Tan).

0734-743X
http://dx.doi.org/10.1016/j.ijimpeng.2013.03.009

Nomenclature

a	half length (longer side) of plate
b	half width (shorter side) of plate
D, q	material strain rate parameters
E	Young's modulus
h	plate thickness
I^*, $\widehat{I}$	non-dimensional impulse and impulse per unit area
l	length of plastic hinge
$m = \rho h$	mass per unit area
$M = \rho abh$	total mass of plate
M_0	fully plastic bending moment
n	material hardening coefficient
t	width of modified boundary condition
t_d	period of blast pulse
T	plate response time under zero period impulse
u, v, w	displacements along x, y, z directions
U^m	membrane strain energy
$V_0 = \widehat{I}/m$	initial velocity
V_{m2}, V_{m3}	transition velocities from mode I → II and mode II → III
w_0, w_f	central deflection before and at failure
$\gamma = a/b$	aspect ratio of plate
γ_c	critical shear strain
Δ^s_{max}	critical shear sliding distance
ε_a, ε_b, ε_e, ε_{rup}	membrane, bending, effective and uniaxial rupture strains
$\dot{\varepsilon}$	strain rate
θ	angular displacement at plastic hinge
κ	curvature
λ	non-dimensional velocity
ν	Poisson's ratio
ρ	density
σ_Y, σ_d	static and dynamic yield strength
ϕ_x, ϕ_y, ϕ_z	rotation about the x, y, z axes
$\chi = b/h$	ratio of half width to thickness of plate
ψ	area fraction of plate detached from boundary

[3–5]. The material description is based on the conventional J_2 plasticity constitutive relation where progressive degradation of material stiffness is introduced through a continuum damage mechanics framework, an approach widely used to model progressive damage and fracture in ductile materials [9,10]. Particular emphasis is placed on addressing the issue of stress convergence in those elements located next to the support, along the plate boundary, where stress singularities may manifest to give unexpected outcomes. Deformation maps are constructed which allow the maximum central deflection of rectangular plates to be read off for different combinations of blast impulse and aspect ratio, and vice-versa.

2. Critical impulse at mode transition – predictions

Nurick and Shave [2] categorised the impulsive response of a square plate according to: mode I (large inelastic deformation), mode II* (through-thickness tearing at the support), mode IIa (complete detachment from support where central deflection *increases* with I^*), mode IIb (complete detachment from support where central deflection *decreases* with I^*) and mode III (failure by shear-band localisation). Experiments by Ramajeyathilagam and Vendhan [6] showed that the impulsive response of rectangular plates with aspect ratio $\gamma > 1$ are broadly similar to the square plates in [2]. In this section, critical impulses corresponding to the transition between deformation modes I → II* and IIb → III are derived. Under the action of an impulsive load, the plate may be assumed to acquire an instantaneous velocity of $V_0 = \widehat{I}/\rho h$ where $\widehat{I}$ is the impulse per unit area, ρ is density and h the plate thickness. Xue and Hutchinson [7] have shown that such an idealisation is valid if the duration of the blast pulse is much shorter compared to the structural response time needed by the plate to reach permanent set. Note that the impulse per unit area $\widehat{I}$ is related to the non-dimensional impulse I^* through

$$I^* = \frac{\widehat{I}}{h\sqrt{\rho\sigma_y}} = \frac{V_0}{\sqrt{\sigma_y/\rho}} \tag{1}$$

where σ_y is the static yield strength of the plate material in uniaxial tension.

2.1. Maximum central displacement – mode I

If $V_0 < V_{m2}$ (critical velocity corresponding to mode I → II* transition), a rectangular plate undergoes permanent inelastic, or mode I, deformation. The theoretical models of Jones [11] and Yu and Chen [12], developed within the constitutive framework of limit analysis, have been shown to predict well the maximum mode I transverse displacement w_0/h of a plate. In general, for a rigid, perfectly-plastic rectangular plate, w_0/h is a dimensionless function of the form

$$\frac{w_0}{h} = \frac{w_0}{h}\left[\lambda\left(=\frac{\rho V_0^2 a^2}{M_0}\right), \gamma\left(=\frac{a}{b}\right)\right], \quad \gamma \geq 1 \tag{2}$$

where h is the plate thickness, $M_0 = \sigma_y h^2/4$ is the fully-plastic bending moment per unit length, σ_y is the static yield strength, V_0 is the instantaneous velocity acquired by the plate, ρ is density, and a and b are the half length and width, respectively, of the plate. For completeness, the results from [11,12] are summarised here.

Ignoring membrane effects, Jones [11] showed that the maximum central deflection of a rectangular plate, with length $2a$ and width $2b$ ($a > b$), subjected to a uniform impulsive velocity V_0 is

$$\frac{w_0}{h} = \frac{(3-\xi_0)\left[(1+\Gamma)^{\frac{1}{2}} - 1\right]}{2[1+(\xi_0-1)(\xi_0-2)]} \tag{3}$$

where $\Gamma = (\lambda/6)(3-2\xi_0)(1/\gamma)^2[1-\xi_0+1/(2-\xi_0)]$ and $\xi_0 = (1/\gamma)[\sqrt{3+(1/\gamma)^2} - (1/\gamma)]$ are both functions of the plate aspect ratio γ and the dimensionless impulse intensity $\lambda = 4I^{*2}\gamma^2\chi^2$, where $\chi = b/h$.

If, however, w_0 approaches or exceeds $O(h)$, then membrane forces become important since it dissipates energy, stiffens the structure and reduces the transverse displacement of the plate significantly. Yu and Chen [12] account for the effects of membrane forces by introducing a kinematically admissible time-dependent velocity field that traces the transient phase of motion of the plates. The temporal evolution of w_0/h are a set of coupled ordinary differential equations (ODEs) that have to be solved numerically using the fourth order Runge-Kutta method.

Table 1
Number of elements in each direction of the uniform-mesh for part 1.

Mesh	Number of elements in z-direction	Number of elements in x- and in y-directions
1	1	21
2	2	42
3	3	63
4	4	84
5	5	105
6	6	126
7	7	147
8	8	168
9	9	189
10	10	210

Both models above do not account for the influence of material strain rate sensitivity and is valid only for aluminium plates since they are relatively rate-insensitive. For strain rate sensitive material, such as mild steel, the static yield stress σ_Y which appears within λ in [11,12] must be replaced with $n\sigma_Y$ where

$$n = 1 + \left(\frac{4V_0 w_0}{3\sqrt{2}Db^2}\right)^{1/q}. \tag{4}$$

Both D and q are material parameters given in Table 2.

2.2. Effective strain distribution

The initiation of plate tearing at the support marks the transition from mode I → II* deformation. To predict the critical velocity corresponding to this transition, the effective strain distribution in the plate must be found. Within the constitutive framework of limit analysis, travelling plastic hinges, or hinge lines, develop in rigid, perfectly-plastic plates along the principal stress-moment directions. Following [4,5,13,14], the total strains ε^t at the hinge is given by

$$\varepsilon^t = \varepsilon^m + \varepsilon^b, \tag{5}$$

where the membrane ε^m and bending ε^b strains are derived separately below.

The membrane strain is derived first by considering a fully-clamped rectangular plate as shown in Fig. 1. Introducing the following non-dimensional coordinates

$$\bar{x} = x/a \quad , \quad \bar{y} = y/b \quad \text{and} \quad \bar{z} = z/h, \tag{6}$$

the displacement profile of the plate, under the action of an out-of-plane (z-direction) loading, is approximated with the following trail functions that satisfy the boundary conditions[15]

$$\begin{aligned} u &= c\sin(\pi\bar{x})\cos\left(\frac{\pi\bar{y}}{2}\right) \\ v &= c\sin(\pi\bar{y})\cos\left(\frac{\pi\bar{x}}{2}\right) \\ w &= w_0\cos\left(\frac{\pi\bar{x}}{2}\right)\cos\left(\frac{\pi\bar{y}}{2}\right) \end{aligned} \tag{7}$$

Table 2
Properties of plate material used in the FE model.

	Density, ρ (kg/m^3)	Young's modulus, E (GPa)	Static yield stress, σ_y (MPa)	Poisson's ratio, ν	D (s^{-1})	q
Al 6061-T6 [23]	2760	69	283	1/3	–	–
Mild steel [2]	7830	197	237	1/3	40.4	5
Mild steel [4]	7830	197	292	1/3	40.4	5

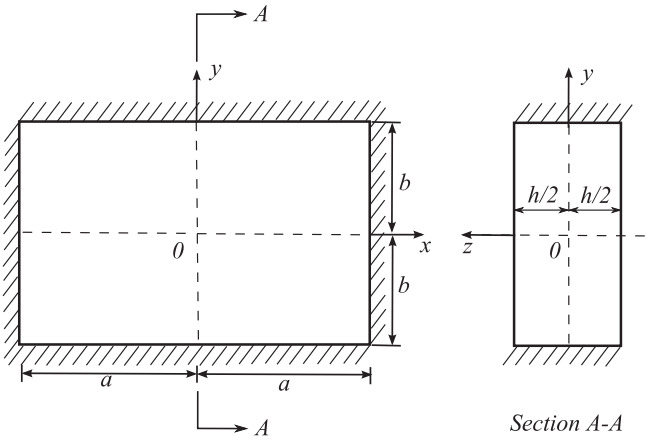

Fig. 1. Schematic of a fully clamped rectangular plate with an aspect ratio of $\gamma > 1$.

where c is an unknown coefficient. The components of the membrane strain in the mid-plane of the plate are found by substituting Eq. (7) into the kinematic relations given by

$$\varepsilon_x^m = u_{,\bar{x}}/a + \left(w_{,\bar{x}}\right)^2/2a^2 \tag{8a}$$

$$\varepsilon_y^m = u_{,\bar{y}}/b + \left(w_{,\bar{y}}\right)^2/2b^2 \tag{8b}$$

$$\gamma_{xy}^m = \left[u_{,\bar{y}}/b + v_{,\bar{x}}/a + w_{,\bar{x}}w_{,\bar{y}}/ab\right] \tag{8c}$$

where $()_{,x} \equiv \partial()/\partial x$. Given that the membrane strain energy is

$$U^m = \frac{Eh}{2(1-\nu^2)}\int\int\left[(\varepsilon_x^m)^2 + (\varepsilon_y^m)^2 + 2\nu\varepsilon_x^m\varepsilon_y^m + \frac{(1-\nu)}{2}\left(\gamma_{xy}^m\right)^2\right]dxdy \tag{9}$$

where $\nu(=1/3)$ is the Poisson's ratio, the unknown coefficient c in Eq. (7) can be found, following the approach of Timoshenko and Krieger[15], by minimising the membrane strain energy with respect to c, i.e.

$$\frac{\partial U^m}{\partial c} = 0, \tag{10}$$

to give

$$c = -\frac{3(a+b)(\pi w_0)^2\left[4(a^2+b^2) - 3ab(1+\nu)\right]}{ab\left[9\pi^2(a^2+b^2)(\nu-9) - 128ab(1+\nu)\right]}. \tag{11}$$

Substituting Eqs. (11) and (7) into Eq. (8) gives the components of the membrane strain along a hinge line.

The bending strain associated with the rotation of the plastic hinge is approximated using [16]

$$\varepsilon^b \cong h\kappa/2 \tag{12}$$

where h is plate thickness and κ is the curvature of the plastic hinge defined as

$$\kappa = \frac{\theta}{l} \tag{13}$$

where θ is the rotational angle of the rigid zones circumscribed by the plastic hinge lines and plate boundary and the hinge length is assumed to be $l = 2h$ in this study [4,5,14].

The effective strain ε_e can be expressed as [16]

$$\varepsilon_e = \frac{1}{3}\sqrt{2\left[(\varepsilon_x^t - \varepsilon_y^t)^2 + (\varepsilon_y^t - \varepsilon_z^t)^2 + (\varepsilon_z^t - \varepsilon_x^t)^2 + \frac{3}{2}\left({\gamma_{xz}^t}^2 + {\gamma_{zy}^t}^2 + {\gamma_{yx}^t}^2\right)\right]}. \tag{14}$$

For a thin plate, it is reasonable to assume that $\varepsilon_z^t = \gamma_{yx}^b = \gamma_{zy}^t = \gamma_{xz}^t = 0$ [17,18]. Substituting the components of the total strain into Eq. (14) leads to a dimensionless function

$$\varepsilon_e = \varepsilon_e\left[\gamma, \nu, \chi\left(=\frac{b}{h}\right), \frac{w_0}{h}, \bar{x}, \bar{y}\right] \tag{15}$$

whereupon the effective strain distribution along each hinge line can be found once γ, χ and w_0/h are specified.

Fig. 2a shows the final hinge pattern in a rigid, perfectly-plastic rectangular plate ($\gamma > 1$) subjected to an impulsive load [11,12]. A square plate, by contrast, develops only two diagonal hinge lines that meet at the origin *0*, i.e. the hinge line labelled 4 does not develop in Fig. 2a. A non-dimensional local coordinate c_{xy} is defined, in accordance to Fig. 2b, as follows

$$c_{xy} = \frac{\sqrt{(x-x_1)^2 + (y-y_1)^2}}{\sqrt{(x_2-x_1)^2 + (y_2-y_1)^2}} \quad , \quad 0 \le c_{xy} \le 1 \tag{16}$$

where (x_1,y_1) and (x_2,y_2) are the start and end coordinates of a hinge line, respectively.

The effective strain in a square plate is found to be greatest next to the mid-point support at $(\bar{x} = 1, \bar{y} = 0)$ and $(\bar{x} = 0, \bar{y} = 1)$ as shown in Fig. 3a. Symmetry dictates that only a quarter of the plate needs to be modelled. Depending on the level of imperfections, tearing could potentially initiate at both, or either, locations. By contrast, Fig. 3b shows that the effective strain in a rectangular plate with aspect ratio $\gamma = 2$ is greatest at the mid-point of its longer side. Fig. 4 gives the effective strain distribution in rectangular plates of different aspect ratios along the clamped edge of $0 \le \bar{x} \le 1$ and $\bar{y} = 1$. Note that the effective strain ε_e is always highest at $(\bar{x} = 0, \bar{y} = 1)$ which is consistent with the location of tear initiation observed experimentally in [6].

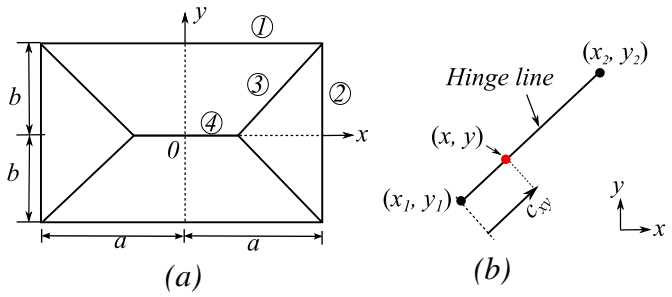

Fig. 2. (a) Final plastic hinge pattern in a rigid, perfectly-plastic rectangular plate where $\gamma > 1$. The four hinge lines for a quarter of the full plate are labelled. (b) A non-dimensional local coordinate c_{xy} along each hinge line.

2.3. Transitional velocities from modes I → II* and IIb → III

Adopting an effective strain failure criterion, through-thickness tearing (mode II*) is assumed to occur when the material ductility is exhausted, i.e. the effective strain reaches the uniaxial rupture strain ε_{rup} of the plate material. Since ε_e is always greatest at $(\bar{x} = 0, \bar{y} = 1)$ for all rectangular plates (quarter model) with aspect ratio $\gamma > 1$, tensile tearing will initiate there. Substituting $\bar{x} = 0$ and $\bar{y} = 1$ into Eq. (15), and replacing ε_e and w_0 with ε_{rup} and w_f, respectively, gives

$$\varepsilon_e\left[\gamma, \nu, \chi, \frac{w_f}{h}\right] = \varepsilon_{rup} \tag{17}$$

whereupon the maximum displacement of the plate w_f/h just before the initiation of tear can be found iteratively. The transitional velocity V_{m2} from mode I → II* follows immediately from Eq. (2). Predictions for V_{m2} are compared with the numerical and experimental results in Section 4.2.

Assuming that the criterion for shear failure in mode III takes the form

$$\Delta_{max}^s = kh \tag{18}$$

where Δ_{max}^s is the critical shear sliding distance and k is a constant obtained by calibration to experiments, Jones [13,16] showed that the transitional velocity V_{m3} corresponding to mode IIb → III deformation may be expressed as

$$V_{m3} = C\sqrt{\frac{\sigma_y}{\rho}}. \tag{19}$$

For beams with a rectangular cross-section where $b/h \gg 1$, V_{m3} is known to be insensitive to geometry but dependent only on material properties [13]. Since a/h and $b/h \gg 1$, it is reasonable to assume that Eq. (19) is also valid for the thin plates studied here. Calibrating Eq. (19) to the experimental data for mild-steel plates in [2] gives $C = 2.39$. The prediction for V_{m3} will be shown to compare well with the numerical results in Section 4.2.

3. Finite element implementation

3.1. FE model and loadings

The numerical analyses are performed using ABAQUS/Explicit®. Full 3D simulations were carried out to model the progressive ductile fracture that occur along, or near to, the plate boundary in experiments [2,6]. All plates modelled have length $2a$ and width $2b$ ($a>b$) if their aspect ratio $\gamma > 1$. If $\gamma = 1$, they have equal length of $2a$ on all sides. Only a quarter of the solid plate is modelled since reflective symmetry exists on two planes along $(\bar{x} = 0, -1/2 \le \bar{z} \le 1/2)$ and $(\bar{y} = 0, -1/2 \le \bar{z} \le 1/2)$. Displacement boundary conditions as shown in Fig. 5b are imposed on both the symmetric planes. Eight 8-node brick elements (C3D8R) with reduced integration and hour-glass control were employed through the thickness of each plate. Convergence studies, see Section 3.2, confirm

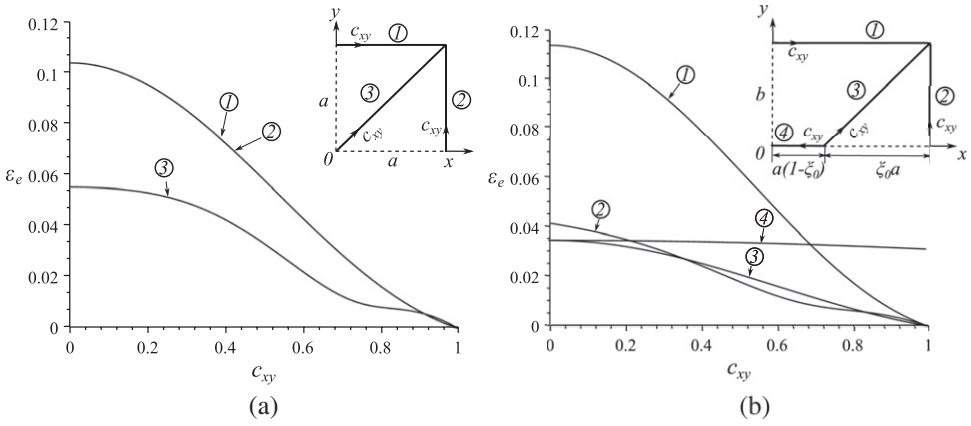

Fig. 3. Effective strain distribution in (a) square ($\gamma = 1$) and (b) rectangular ($\gamma = 2$) mild-steel plates (see Table 2 for material properties) subjected to identical zero-period impulse per unit area of $\hat{I} = 167.4$ Ns/m^2 ($I^* = 0.0768$). Their corresponding maximum transverse displacements are $w_0/h = 8.75$ and $w_0/h = 4.6$, respectively. Note that $a = 0.0445$ m and $h = 0.0016$ m for both plates. (a) [$\gamma = 1$] (b) [$\gamma = 2$].

that this is sufficient to capture necking localisation, progressive damage and ductile fracture with acceptable fidelity.

Xue and Hutchinson [7,8] have shown that the impulsive blast response of a structure is sensitive to the response time T needed to attain maximum deflection for a zero-period impulse. This time scale determines whether it is acceptable to idealise a finite-period loading as a zero-period impulse, i.e. the plate acquires an instantaneous initial velocity of $V_0 = \hat{I}/m$. The response time of the square plate in the experiments of Nurick and Shave [2], with dimensions $0.089(2a) \times 0.089(2b) \times 0.0016(h)$ m and material properties given in Table 2, is found numerically to be 120 μs. Since the typical blast duration is $t_d = 15$ μs in [2], the loading imparted by the blast pulse may be idealised as a zero-period, *uniform-momentum* impulse because $t_d/T = 0.125 \ll 1$. In a similar vein, since the response time of the rectangular plates are also of the same order of magnitude as the square plates in [2], assuming that the blast duration remains at $t_d \approx 15$ μs, the zero-period idealisation would remain valid.

3.2. Boundary, or support, conditions

Fig. 5a gives the standard fully-clamped boundary condition (BC) used by existing numerical studies in [2,5,6,14]. It can be shown that key local stresses at the plate boundary do not converge with repeated mesh refinement due to stress singularities [19–21]. To accurately model progressive ductile fracture along the boundary of the plate, a modified BC given in Fig. 5b is used here [21,22]. The asymptotic identification of stress singularities in structural dynamics problem will be pursued elsewhere in [22]. Here, it suffices to demonstrate that both the standard and modified BCs predict nearly identical central deflection for the plates, but only the latter gives converged local stresses along the plate boundary. The efficacy of the modified BC is further demonstrated in Section 4 by the excellent agreement between the predicted maximum plate deflection by the FE model and the experimental results of [2,4].

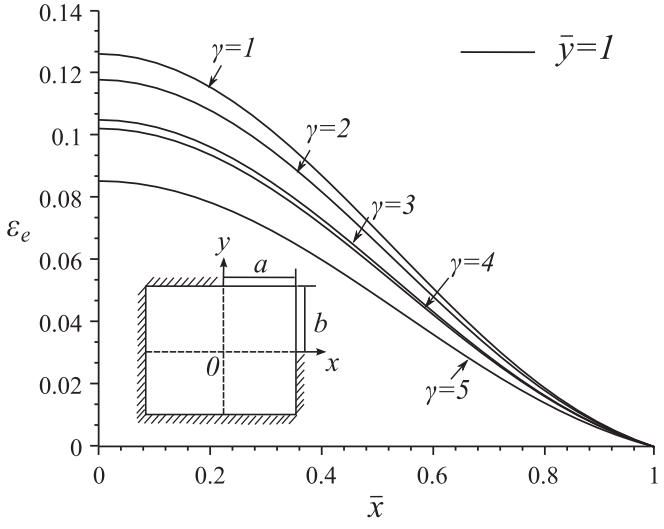

Fig. 4. Effective strain distribution on the longer edge of rectangular mild-steel plates with different aspect ratios. All plates have identical material properties subjected to the same loading as in Fig. 3.

Three additional parts (parts 2–4 and parts 5–7) are added to each side of the original solid plate (part-1) to form an extended boundary as shown in Fig. 5b. Note that the standard fully-clamped BC of Fig. 5a are imposed on parts 4 and 7. All the additional parts have equal width τ and identical material properties as the solid plate, apart from a gradation of their elastic modulus E, by a factor α. Symmetric BCs are applied, just like to the solid plate. The parameters $\tau = h/6$ and $\alpha = 10$ are obtained by calibration to the experimental data of Nurick and Shave [2].

Fig. 6 plots the predicted maximum in-plane stress σ_{yy} and equivalent plastic strain $\bar{\varepsilon}^{pl}$ for different mesh density used in part-1. The number of elements along each direction of the uniform-mesh is listed in Table 1. For a square plate without imperfections, the maximum values for σ_{yy} and $\bar{\varepsilon}^{pl}$ are found at $(\bar{x} = 1, \bar{y} = 0)$ and $(\bar{x} = 0, \bar{y} = 1)$ where tearing is expected to initiate from either, or both, locations. It is evident that σ_{yy} and $\bar{\varepsilon}^{pl}$ do not converge for the standard BCs shown in Fig. 5a. Instead, convergence is achieved with the modified BCs. Fig. 6 shows that mesh size No.8 gives sufficiently accurate results and is used here.

Fig. 7a shows that the differences between the predicted deflection profiles by the two BCs are negligibly small. Similarly, for the time-history of their central deflections as shown in Fig. 7b. In general, w_0/h are unaffected by the presence of stress singularities at the boundary; therefore, evaluation of performances, based on maximum transverse deflection of the plates, lead to identical conclusions for either BCs provided necking localisation and ductile fracture did not intervene.

Since only the solid plate (part 1) acquires a uniform velocity, a proportion of the internal and plastic energies are absorbed by the extended boundary (parts 2–7). Fig. 8 gives the time history of the energies dissipated. It shows that no more than 15% of the initial kinetic energy, acquired by part 1, is absorbed by the extended boundary throughout the entire response duration. Although this

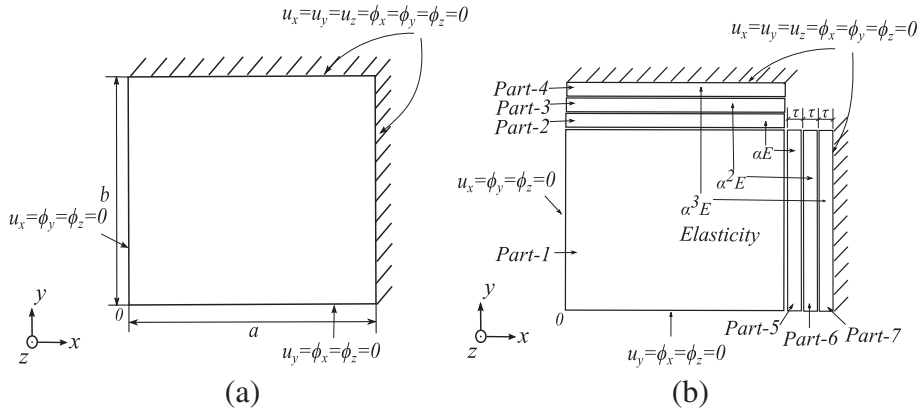

Fig. 5. (a) Fully-clamped and (b) modified boundary conditions adopted in this study. u and ϕ refers to displacement and rotational degree of freedom, respectively, in the direction indicated by their subscript. $a > b$ for rectangular and $b = a$ for square plates.

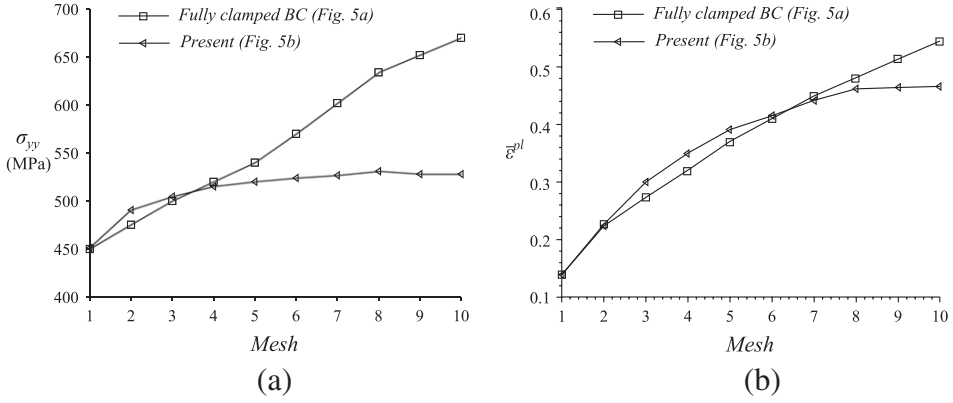

Fig. 6. Predicted maximum (a) in-plane stress σ_{yy} and (b) equivalent plastic strain $\bar{\varepsilon}^{pl}$ at $(\bar{x} = 1, \bar{y} = 0)$ and $(\bar{x} = 0, \bar{y} = 1)$. Results are for square mild-steel plate of dimensions $0.089(2a) \times 0.089(2b) \times 0.0016(h)$ m subjected to a non-dimensional impulse of $I^* = 0.632$ (or $\hat{I} = 1378$ Ns/m^2).

would lead to a somewhat smaller final plate deflection in mode I, the good comparison between FE predictions and experimental results in [2,4] suggests that the level of energy loss is acceptable.

3.3. Materials and damage models

3.3.1. Plate materials

Two plate materials are modelled in this study aluminium (6061-T6) and mild-steel; both have existing experimental data on their impulsive response [2,4,23]. Table 2 lists the properties of the respective plate material. Notice that the static yield strength of mild-steel used in [4] is slightly higher than in [2].

The material description adopted is based on the conventional J_2 plasticity constitutive relation with isotropic hardening. Material strain rate sensitivity is accounted for through a dynamic flow stress, evaluated at a uniaxial plastic strain rate $\dot{\varepsilon}$, by adopting the Cowper-Symonds constitutive relation [16]

$$\sigma_{dy} = \sigma_y \left(1 + \left|\frac{\dot{\varepsilon}}{D}\right|^{1/q}\right). \tag{20}$$

Both D and q are material parameters given in Table 2. The aluminium plates are assumed to be rate-insensitive.

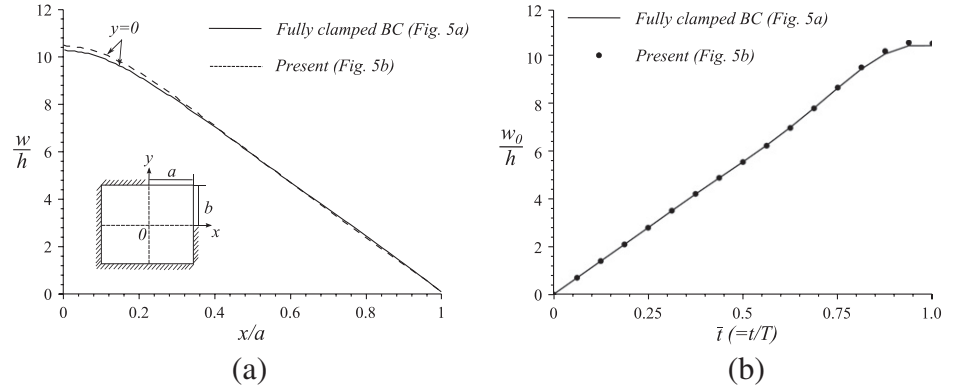

Fig. 7. (a) Deflection profile along the x-axis (the same for y-axis due to symmetry) and (b) time-history of the central deflection of the plate. Results are for square mild-steel plate of dimensions $0.089(2a) \times 0.089(2b) \times 0.0016(h)$ m and subjected to a non-dimensional impulse of $I^* = 0.632$ (or $\hat{I} = 1378$ Ns/m^2).

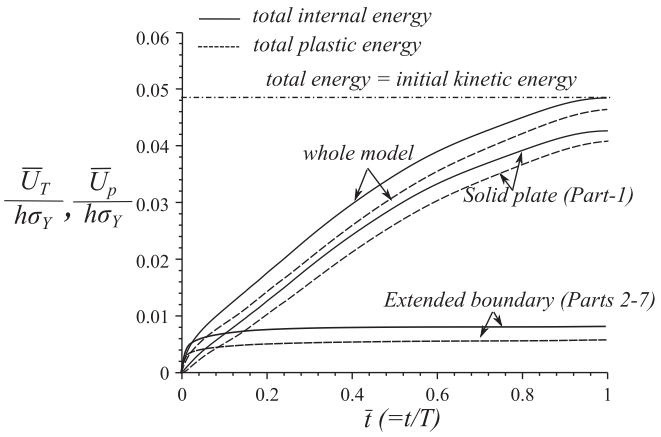

Fig. 8. Time history for the dissipation of non-dimensional internal $(\overline{U}_T/h\sigma_y)$ and plastic $(\overline{U}_p/h\sigma_y)$ energies by a square mild-steel plate of dimensions $0.089(2a) \times 0.089(2b) \times 0.0016(h)$ m subjected to a non-dimensional impulse $I^* = 0.632$ (or $\hat{I} = 1378$ Ns/m^2).

Table 3
Material parameters used by the damage model.

Damage model	$\bar{\varepsilon}_d^{pl}$ or $\bar{\varepsilon}_s^{pl}$	$\bar{\varepsilon}_f^{pl}$	$\overline{u}_f^{pl}$
Ductile	0.2	0.55	0.00011
Shear	0.2	0.4	0.00008

3.3.2. Damage criteria and evolution [24]

Failure of solid plates subjected to impulsive loading can be attributed to two competing bulk material failure mechanisms, viz. ductile fracture and/or shear band localisation [2,4,23]. The progressive damage model for ductile materials in ABAQUS/Explicit is used here.

The criteria for initiation of ductile (ω_d) and shear (ω_s) damage in the FE model are given by

$$\omega_d = \int \frac{d\bar{\varepsilon}^{pl}}{\bar{\varepsilon}_d^{pl}\left(\eta, \dot{\bar{\varepsilon}}^{pl}\right)} = 1 \text{ and } \omega_s = \int \frac{d\bar{\varepsilon}^{pl}}{\bar{\varepsilon}_s^{pl}\left(\theta_s, \dot{\bar{\varepsilon}}^{pl}\right)} = 1 \tag{21}$$

where ω_d and ω_s are state variables that increases monotonically with the incremental change in equivalent plastic strain. Here, the equivalent plastic strains $\bar{\varepsilon}_d^{pl}$ (at the onset of ductile damage) and $\bar{\varepsilon}_s^{pl}$ (at the onset of shear damage) are assumed, respectively, to be a function of stress triaxiality η and strain rate $\dot{\bar{\varepsilon}}^{pl}$; and, a function of the shear stress ratio θ_s and strain rate $\dot{\bar{\varepsilon}}^{pl}$. When the criteria in Eqn. (21) are met, a damage evolution law is defined for each criterion, in terms of the effective plastic displacement $\dot{\overline{u}}^{pl}$ as follows [24]

$$\dot{\overline{u}}^{pl} = L\dot{\bar{\varepsilon}}^{pl} \tag{22}$$

where $L = 2 \times 10^{-4}$ m is the characteristic length of the first-order element used in the present FE model. Assuming a linear relationship exists between the evolution of the damage variable d and the effective plastic displacement $\dot{\overline{u}}^{pl}$, the damage variable would increase according to [24]

$$\dot{d} = \frac{L\dot{\bar{\varepsilon}}^{pl}}{\overline{u}_f^{pl}} = \frac{\dot{\overline{u}}^{pl}}{\overline{u}_f^{pl}} \tag{23}$$

where $\overline{u}_f^{pl}$ is the effective plastic displacement at failure given in Table 3. For simplicity, it is assumed that the damage associated with each criterion contributes to the overall damage variable in a maximum sense, which is the default used in ABAQUS. In the present study, any element where their material stiffness is fully degraded, i.e. $d = 1$, is deleted from the mesh. Whilst it may be argued that element deletion leads to a loss of mass which will affect the impulsive response of the plate, it was found not to affect the results significantly since less than 5% of the total number of elements are deleted in each of the plate modelled here.

Table 3 lists the parameters used in the damage models. Note that the parameters for shear damage are obtained by calibration to the experimental data of Nurick and Shave [2].

4. Validation of analytical and numerical predictions against experiments

In this section, the analytical and FE predictions are validated against experimental data for square mild-steel [2,4] and rectangular aluminium [23] plates. Note that the blast loadings in [2,4,23] may also be idealised as zero-period impulses. The aluminium plates in [23] have dimensions $0.1286(2a) \times 0.0763(2b) \times h$ m, with a range of thickness h. The square mild-steel plate specimens used in [2,4] have dimensions of $0.098(2a) \times 0.098(2b) \times 0.0016$ m. The properties for the two different plate materials are listed in Table 2. Only the mode I central deflection are available in [23] whilst data on all three modes of deformation are provided in [2,4].

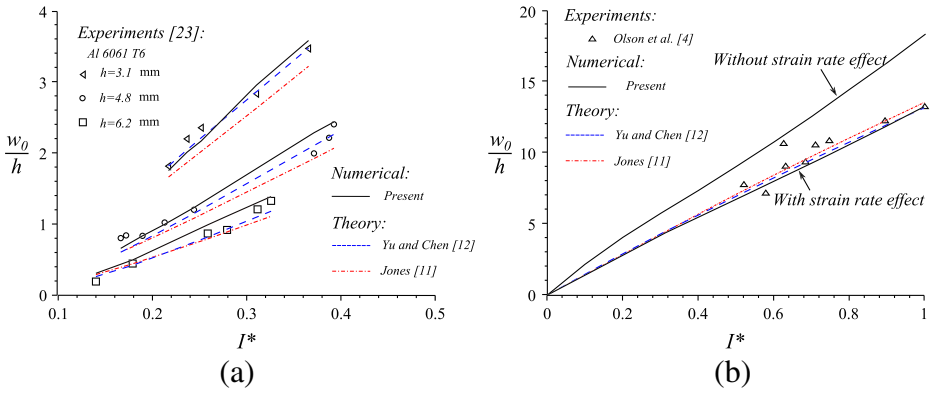

Fig. 9. Comparison of the mode I central deflection for (a) aluminium [23] and (b) mild steel [4] plates with FE and theoretical predictions at different levels of I^*. The aluminium and mild-steel plates has an aspect ratio of $\gamma = 1.685$ and $\gamma = 1$, respectively.

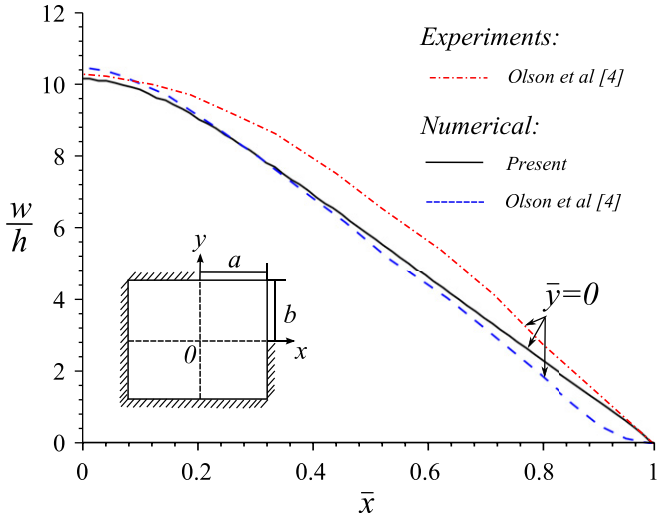

Fig. 10. Deflection profile of a mild steel plate ($\gamma = 1$) subjected to an impulsive load per unit area of $\hat{I} = 1872$ Ns/m^2 (or $I^* = 0.86$).

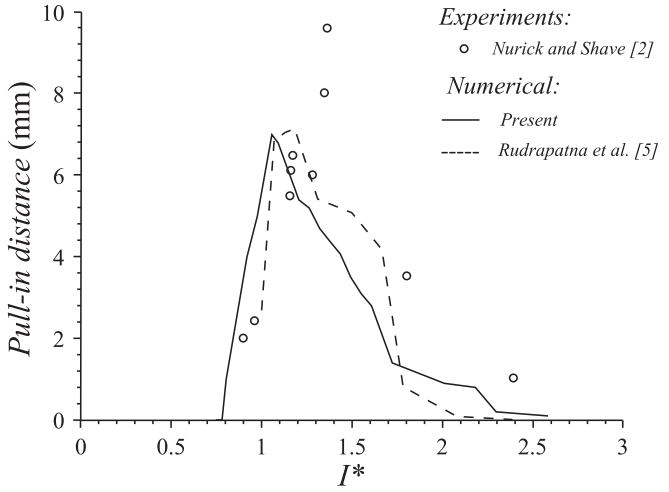

Fig. 12. Side pull-in distance versus non-dimensional impulse for mild-steel plates ($\gamma = 1$).

4.1. Maximum plate deflection

Fig. 9a shows that the mode I central deflection is in good agreement with the theoretical predictions by Yu and Chen [12]; in particular, for the thinner specimen ($h = 3.1$ mm) where membrane effects are dominant. The modified BC appears to better predict the central deflection of the thicker plate specimens ($h = 6.2$ mm). This is because relaxation of the in-plane and out-of-plane degree of freedom at the plate boundary, gives a somewhat larger w_0/h than the standard BC would otherwise allow. Failure to account for material strain rate sensitivity would lead to over-prediction of w_0/h with I^* as shown in Fig. 9b. In general, there is good agreement between experiment data and the current FE predictions.

Fig. 10 plots the deflection profile along $\bar{y} = 0$ for a square mild steel plate subjected to a non-dimensional impulse $I^* = 0.86$. Its central deflection is well predicted by the current FE model. This lends further support to the contention that replacing the standard BC with the modified one in Fig. 5b has hardly any effect upon the central deflection of the plate. Note, however, that discrepancies in the deflection profiles are observed away from $\bar{x} = 0$. As $\bar{x} \to 1$, the modified BC give a better prediction of the deformed plate profile compared to the standard one, again, because the former relaxes the in-plane and out-of-plane degree of freedom along the boundary.

The predicted central deflection is compared to the experimental data of Nurick and Shave [2] where there is a good agreement, see Fig. 11. Furthermore, the FE model successfully predicts a reduction in w_0/h with increasing I^* for a plate deforming in mode IIb. The observed discrepancy between FE predictions and experimental data for mode IIb is because the former records the central deflection of the plate just before it completely detaches from the support unlike in the latter.

Nurick and Shave [2] reported that, for mode II*, the plate tears away from the support resulting in 'pulling-in' of the mid-side of the plate. This 'pulling-in' distance increases initially with I^* but reduces when the maximum plate deflection is reached. The

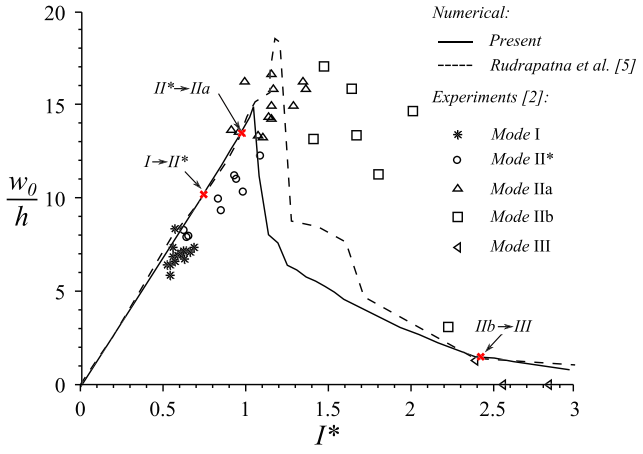

Fig. 11. Comparison of the numerical central (maximum) deflection with the experimental data at different levels of I^*. Each red cross indicates a transition in deformation mode predicted by the current FE model. All plates have aspect ratio of $\gamma = 1$. (For interpretation of the references to colour in this figure legend, the reader is referred to the web version of this article.)

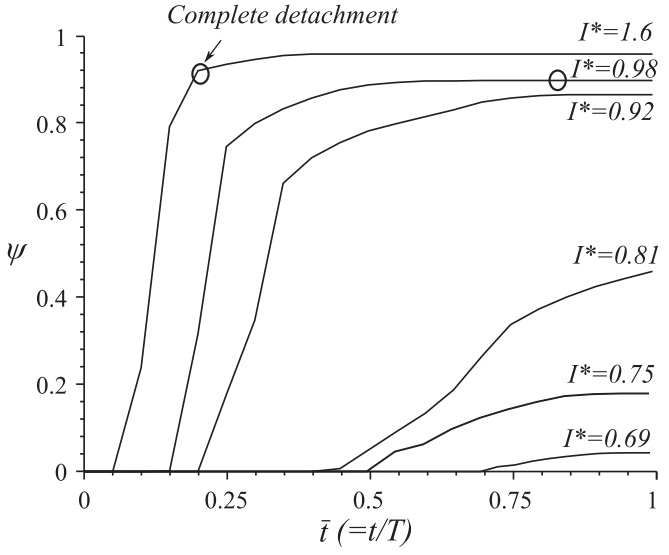

Fig. 13. Time history of ψ for different levels of I^*. ○ indicates the instant when plate is completely detached from its support. Results shown are for a square mild-steel plate with properties listed in Table 2 with a response time of $T = 120$ μs.

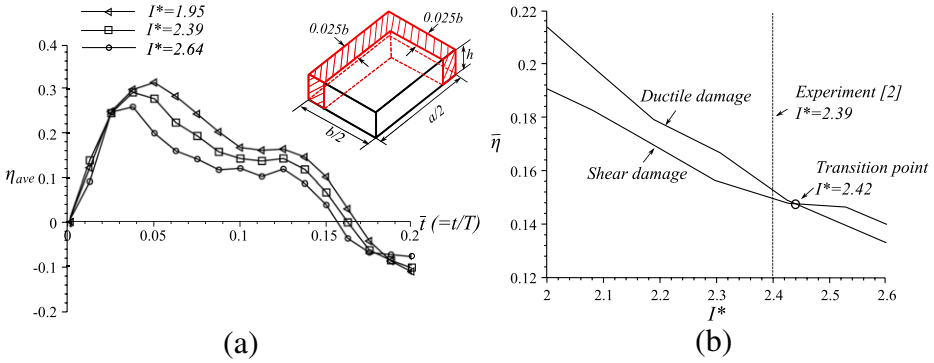

Fig. 14. (a) Time history of stress triaxiality, η_{ave}, averaged over all elements in the shaded region, and (b) Comparison of the time-averaged stress triaxiality $\bar{\eta}$ for a plate using the ductile and shear damage model. Results shown are for a square mild-steel plate with properties listed in Table 2 with a response time of $T = 120\ \mu s$.

general trend of the 'pull-in' distance with I^* is well predicted by the current FE model in Fig. 12. The observed discrepancies are due to the same reason given previously for Fig. 11.

4.2. Critical impulses corresponding to mode transitions

A non-dimensional parameter ψ is introduced to quantify the area fraction of plate that has become detached from the support as follows

$$\psi = \frac{\textit{Area of plate periphery detached from the support}}{\textit{Total area of plate periphery attached to support}[\,=2ha \text{ or } 2hb)]}. \tag{24}$$

Since the mesh is uniform, the numerator of Eq. (24) is easily calculated by multiplying the total number of deleted elements to the surface area of the side of an 8-node brick element which is attached to the support. For a square plate, ψ is identical on all sides due to symmetry. If $\psi = 0$, no elements are deleted, i.e. the plate deforms in mode I. Conversely, if $\psi = 1$, all elements along the plate periphery are deleted.

Fig. 13 gives the time-history of ψ at different values of I^* for a typical square mild-steel plate in [2]. The FE model predicts that an element is first deleted at $I^* = 0.69$ (it would *not* be possible to verify this experimentally) and through-thickness tearing occurs at a higher impulse of $I^* = 0.75$. Complete detachment from the support occurs whenever $I^* \geq 0.98$, i.e. the critical impulse at mode II* → IIa transition is $I^* = 0.98$. With increasing I^*, complete detachment occurs at increasingly earlier times of t/T as expected. Notice that ψ is always less than unity even for high levels of impulse due to crack branching away from the boundary into the plate's interior. This will become clearer in Section 5.1.

A procedure to determine the critical impulse corresponding to mode IIb → III transition is now described. Fig. 14a shows the time history of three typical stress triaxiality curves $\eta_{ave}(\bar{t})$; they are obtained by averaging the stress triaxiality of all the elements in the shaded region as shown. The width of $0.025b$ is chosen so that it covers the region of the plate where the cracks may conceivably propagate. Note that beyond $\bar{t}_0$, the non-dimensional time corresponding to $\eta_{ave} = 0$, the plate is completely detached from its support. Conversely, if I^* is insufficient to cause complete detachment, then η_{ave} is always greater than zero. At each impulse level, the time-averaged value of the function $\eta_{ave}(\bar{t})$, defined as

$$\bar{\eta} = \frac{\int_0^{\bar{t}_0} \eta_{ave}(\bar{t})\,\mathrm{d}\bar{t}}{\bar{t}_0}, \tag{25}$$

is obtained for the two different damage models, viz. ductile and shear, applied separately to give the curves shown in Fig. 14b. A unique cross-over point can be identified which determines the transition from mode IIb → III. Beyond this cross-over point, only the shear damage model is used; otherwise, the ductile damage model is applied in a maximum sense alluded to in Section 3.3.2. Using this proposed criterion, Table 4 compares the theoretical and numerical critical impulses (and transitional velocities) with their experimental counterpart in the literature. The predictions, by FE and theory (Eqs. (17) and (19)), are in good agreement with the experimental data in [2] and [4]. The predicted critical impulse is sensitive to the parameters α and τ of the modified BC (Fig. 5b). Since the FE model is calibrated to experimental data where the plate remains attached to the support, the predicted critical impulse for mode IIa → IIb transition is much lower than that observed experimentally.

Table 4
Critical impulses I^* (and velocities V_0, m/s) corresponding to mode transitions.

Mode	Theory Eqn. (17) or (19)	FE (Present)	FE[5]	Experiments[2]	Experiments[4]
I → II*	0.78 (135.4)	0.75 (130.0)	0.97 (168.8)	0.62 (108.8)	–
II* → IIa	–	0.98 (172.0)	1.02 (177.5)	0.98 (171.3)	1.11 (193.5)
IIa → IIb	–	1.05 (184.0)	1.27 (221.0)	1.48 (257.0)	1.45 (251.9)
IIb → III	2.39 (416.2)	2.42 (421.0)	2.32 (404.7)	2.39 (416.2)	–

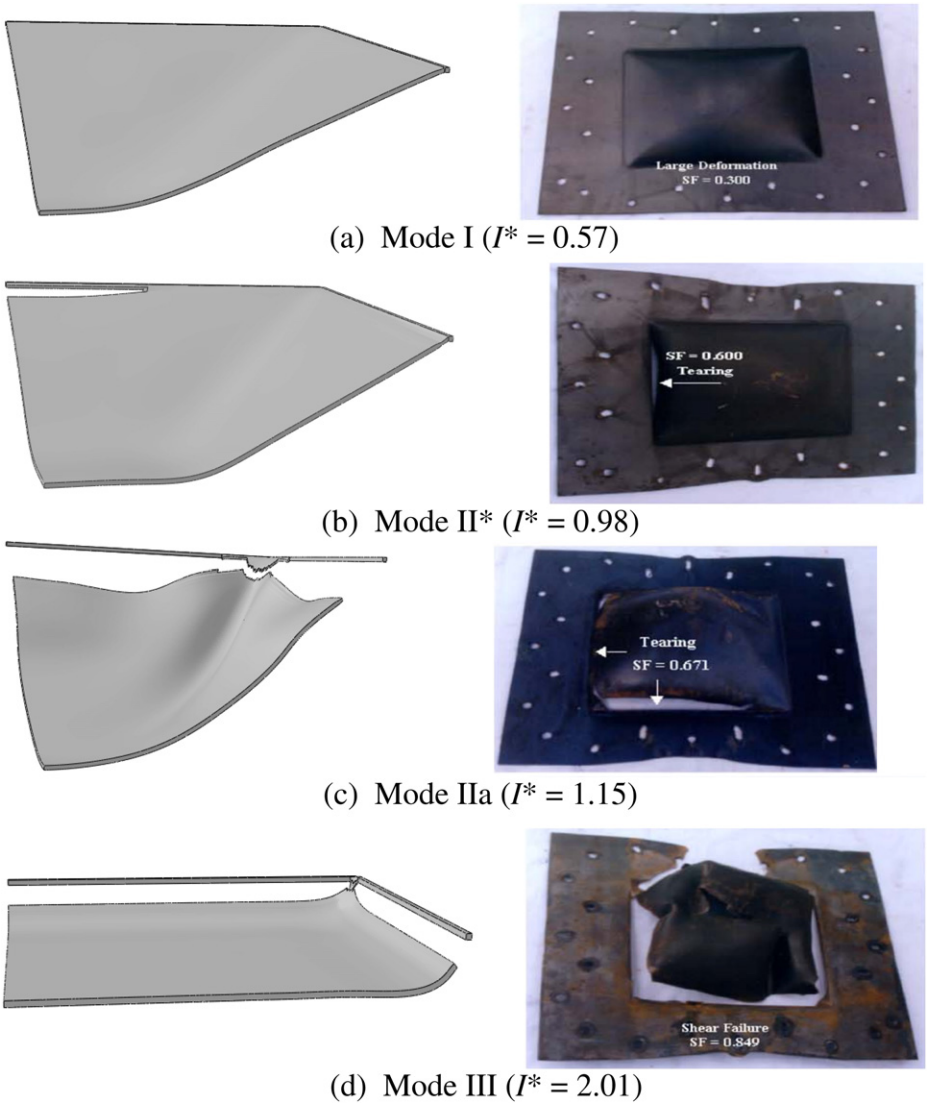

Fig. 15. Comparison of predicted deformation modes (left column) for rectangular mild-steel plates ($\gamma = 1.2$) to the 'post-test' specimens (right column) of Ramajeyathilagam and Vendhan [6]. Note that the former shows a quarter of the rectangular plate due to symmetry. Properties of the mild-steel plates in [6] are as follows: $\rho = 7860$ kg/m^3, $E = 210$ GPa, $\sigma_y = 300$ MPa and the rests are identical to Table 2.

5. Predicted impulsive response for rectangular plates

The fully validated FE model of the previous section is now employed to compute the zero-period impulsive response of rectangular plates with aspect ratio ranging between $2 \leq \gamma \leq 5$. All rectangular mild-steel plates modelled have the same total mass as the square ones ($M = 0.0992$ kg) used by Nurick and Shave [2]. Likewise, for their material properties listed in Table 2. The results

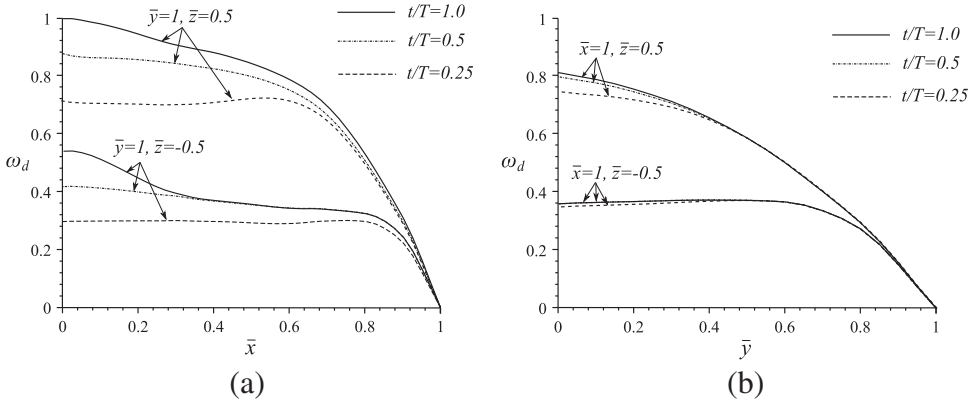

Fig. 16. Ductile damage state variable ω_d for a rectangular plate with aspect ratio $\gamma = 2$ subjected to an impulse $I^* = 0.55$. The plate is deforming in mode I.

for square mild-steel plates from [2] are also included for comparison.

5.1. Deformation modes

Fig. 15 shows that the current FE model successfully captures the different modes of impulsive response observed in a typical rectangular plate ($\gamma = 1.2$). Comparison is made here to the 'post-test' specimens of [6] where a set of clear photographs are available, instead of with those in [2,4]. The zero-period, *uniform-momentum* idealisation is also valid in [6]. For rectangular plates deforming in modes IIa and IIb, a crack propagates along each side of the plate boundary. At some point, their crack paths are deflected inwards, circumventing the corner of the plate. When the two crack paths meet, complete plate detachment occurs. It is not entirely clear why the crack path deviates from the plate boundary as it approaches the corner although this occurs irrespective of the value of the aspect ratio. This is the reason why ψ is always less than unity in Fig. 13 regardless of the value of I^*.

Fig. 16 shows the distribution of the state variable ω_d for a typical rectangular plate ($\gamma = 2$) subjected to a non-dimensional impulse $I^* = 0.55$. When $\omega_d = 1$, the material stiffness at that point begins to degrade in accordance to the evolution law given in Eqn. (22). It is noteworthy that ductile damage, by nucleation, growth and coalescence of voids, initiates well before the transition from mode I → II*. Current simulations showed that the first element to be deleted, i.e. the material point where its stiffness is fully degraded, always occurs at ($\bar{x} = 0, \bar{y} = 1, \bar{z} = 0.5$), on the surface incident to the blast irrespective of I^*. It is, therefore, surprising to see in Fig. 15b (right-side image) that tearing appears to initiate on the shorter side of the plate in [6]. This experimental anomaly must be due to material and/or geometric imperfections since it was, also, predicted that tearing must initiate at the mid-point of the longer side by the total and/or effective strain theory of [6].

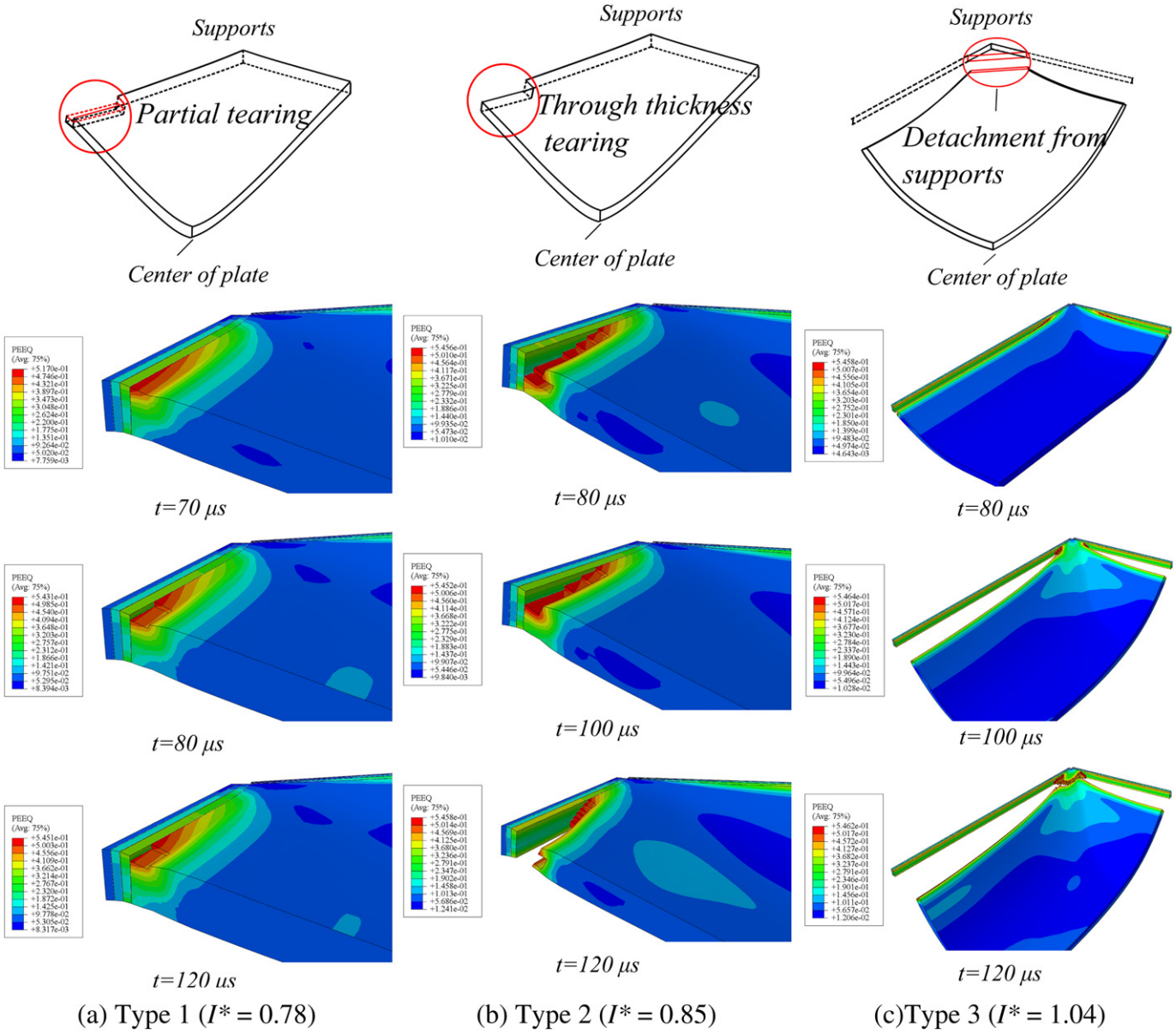

Fig. 17. Time evolution of the equivalent plastic strain contour in a rectangular plate ($\gamma = 2$) and the three types of mode II response predicted by the current FE model.

5.2. Types of mode II response

The mode II response of a plate was previously categorised as mode II* (through-thickness tearing at the support), mode IIa (complete detachment from support where central deflection *increases* with I^*) and mode IIb (complete detachment from support where central deflection *decreases* with I^*) [2]. However, the current FE simulations showed that non-through-thickness tearing typically precedes mode II*. In light of this, it is advantageous to reclassify the mode II response into three distinct types according to the magnitude of the non-dimensional impulse I^*, viz. Type 1 (non-through-thickness tearing), Type 2 (through-thickness tearing) and Type 3 (complete detachment from support). As a result of this reclassification, the prediction by Eq. (17) should now be for mode II(Type 1) → II(Type 2).

Fig. 17 shows the equivalent plastic strain contour for a rectangular plate ($\gamma = 2$) subjected to different levels of impulse. At $I^* = 0.78$, Fig. 17a shows that non-through-thickness tearing occurs along the support, referred to as a Type 1 response hereinafter. As predicted in Section 2.3, the first element to be deleted occurs at $(\bar{x} = 0, \bar{y} = 1, \bar{z} = 0.5)$, on the incident face along the mid-point of the longer side of the plate. By contrast, Type 2 response entails through-thickness tearing of the plate at the support as depicted in Fig. 17b. Fig. 17c shows a typical Type 3 response where I^* is sufficiently large for complete detachment of the plate to occur. Notice the plate remnant at the corner of the support caused by the deviation of the crack paths (Fig. 17c) which is also evident in the experimental results shown in Fig. 15c.

5.3. Failure maps

To ensure that comparison is made between plates of equal total mass and thickness, the aspect ratio (defined as the ratio of the longer to shorter side) is varied by choosing the longer and shorter sides of the plate to have length of $a\sqrt{\gamma}$ and $a/\sqrt{\gamma}$, respectively, where a (= 0.0445 m) is the half length of the square plate in [2]. In this manner, the plate thickness (h = 1.6 mm) and plate mass (M = 0.0992 kg) remain equal between plates of different aspect ratio γ. Fig. 18 shows how the non-dimensional central deflection w_0/h varies with I^* for different aspect ratios ranging from $1 \le \gamma \le 5$. Analytical prediction of the critical impulses corresponding to the transition from mode I → II(Type 1) and from mode II(Type 3) → III are indicated by the two dash-dot lines. The overall trend of the central deflection with I^* is broadly similar to a square plate. For a plate deforming in modes I or II(Type 1 and 2), its central deflection reduces with increasing γ at a given I^*. By contrast, w_0/h is insensitive to γ. The increasing-decreasing trend of w_0/h with I^* is clearly evident in the mode II(Type 3) response.

There is an excellent agreement between the mode I central deflection and the theoretical predictions of Yu and Chen [12]. Equation (17) under predicts the transitional impulse at mode I → II(Type 1) because of the different constitutive assumption used in the formulation of the analytical prediction and in the FE model. The former is based on the constitutive framework of limit analysis resulting in a higher w_0/h than the latter which considers isotropic hardening. Consequently, a plate made of a rigid-perfectly plastic material would fail at a lower I^* as seen in Fig. 18. Both the FE results and theory predict that the critical impulse at mode I → II(Type1) transition increases with aspect ratio γ. By contrast, the transition at mode II(Type 3) → III is insensitive to plate geometry but depends only on material properties and is well predicted by Eq. (19)

Fig. 19 shows a deformation map, constructed from the data in Fig. 18. The contours of dotted line join constant value of w_0/h within that particular mode of deformation. This gives a map which

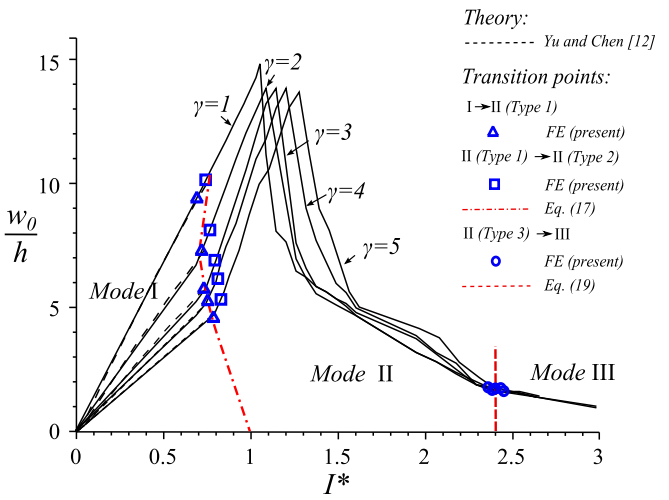

Fig. 18. Variation of the maximum mid-point deflection with non-dimensional impulse I^* for rectangular plates with different aspect ratio. All the plates shown have the same thickness h = 1.6 mm and a total mass of M = 0.0992 kg.

is really useful to designers. Any pair of values of I^* and γ now locates a point on the map. From the map, one can determine the deformation mode and read off the mid-point deflection of the plate (by interpolation using two known values if required). Alternatively, it allows a designer to determine the critical non-dimensional impulse I^*delineating different modes of deformation, and the corresponding central deflection of the plate, at a given aspect ratio γ. Note that the map assumes zero-period impulsive load (i.e. $t_d/T = 0$). For the corresponding finite-period loading case (i.e. $t_d/T \neq 0$), one would expect a lower central deflection at the same I^* and the boundaries in the deformation map of Fig. 19 will change. This is explored in the next section for the case of a square plate.

Previously in Fig. 19, the mass per unit area $m(=\rho h)$ of all the plates were kept constant at m = 12.53 kg/m^2. Let this be increased by a factor $k > 1$, from ρh to $\rho k h$. To keep the same mass of M = 0.0992 kg between plates, its longer and shorter sides must be reduced accordingly to $a/\sqrt{k}$ and $b/\sqrt{k}$, respectively. The effects of plate thickness (or mass per unit area m) upon the deformation mode are explored in this manner. Fig. 20a shows how the boundaries, delineating the different modes, shift with the factor k. For a given γ, the critical impulse I^* corresponding to the transition from mode I → II(Types 1 + 2) and from mode II(Types 1 + 2) → II(Type 3) increases with plate thickness. By contrast, the

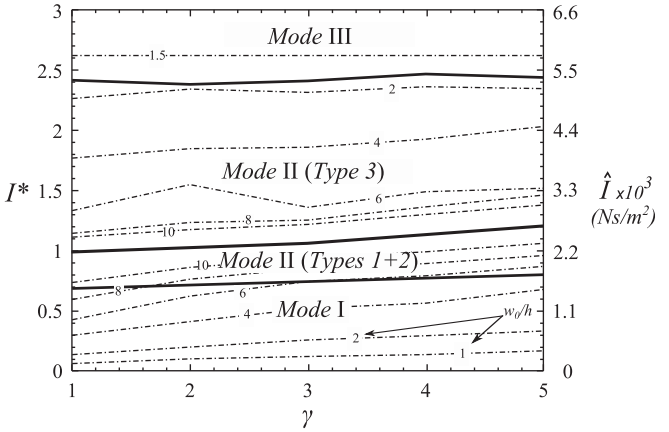

Fig. 19. Deformation map for a rectangular mild-steel plate with a constant mass per unit area of m = 12.53 kg/m^2 and a total mass of M = 0.0992 kg.

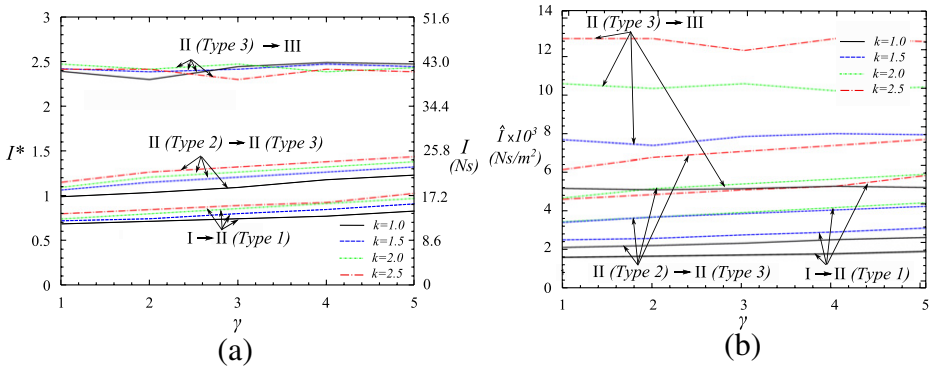

Fig. 20. Deformation maps showing the changing boundaries according to different plate thickness h.

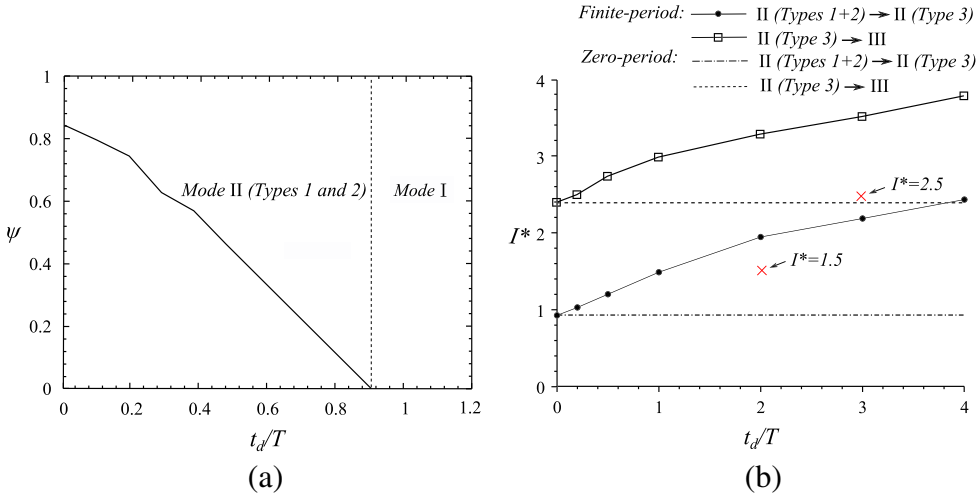

Fig. 21. (a) Influence of blast duration t_d/T upon the area fraction of plate ψ that becomes detached from the support; (b) Effects of the blast duration upon the boundaries corresponding to the transition from mode II(Types 1 + 2) → II(Type 3) and from mode II(Type 3) → III. Results shown are for square mild-steel plate subjected to a non-dimensional impulse of $I^* = 0.92$.

boundaries corresponding to mode II(Type 3) → III transition do not appear to change significantly which is consistent with the fact that the corresponding transitional impulse I^* depends only on material properties. On the other hand, Fig. 20b re-plots the deformation map for $\hat{I}$ (impulse per unit area) versus γ. Increasing k (or the plate thickness) leads to a corresponding increase in $\hat{I}$ (see Eq. (1)) which is consistent with Fig. 20b.

5.4. Effects of finite-period impulse upon the failure mode

Xue and Hutchinson [7,8] have previously shown that the ratio of the blast duration to the overall response time of the structure (t_d/T) determines whether the blast loading may be approximated as a zero-period, *uniform-momentum* impulse. In this section, results from numerical simulations are presented which examine the influence of t_d/T upon the deformation mode of square mild-steel plates.

Fig. 21a shows the effect of increasing t_d/T upon the area fraction of plate (ψ) that becomes detached from the support. Note that the plate is loaded by a zero-period impulse at $t_d/T = 0$. The results show that for the same non-dimensional impulse of $I^* = 0.92$, ψ decreases with increasing blast duration. If $t_d/T > 0.9$, the mode of deformation switches from mode II(Types 1 or 2) to mode I. Hence, the response of the plate is also dependent upon the non-dimensional blast duration t_d/T.

Fig. 21b shows how the boundaries corresponding to the transition from mode II(Types 1 + 2) → II(Type 3) and from mode II(Type 3) → III shifts in accordance to the blast duration. Increasing the blast duration has an effect of delaying the transition between deformation modes. For instance, a square plate which was previously deforming in mode II(Type 3) at $I^* = 1.5$, under the action of a zero-period impulse, now deforms in mode II(Type 1 or 2) if $t_d/T \geq 2.0$. In a similar vein, the plate deforms in mode II(Type 3) instead of mode III at $I^* = 2.5$ if $t_d/T \geq 3.0$. It is not unreasonable to expect the blast response of the rectangular plates to be similarly affected by the non-dimensional blast duration t_d/T; its detailed study will be reported elsewhere.

6. Conclusions

A fully-validated FE model has been presented which is capable of modelling the impulsive response of rectangular mild-steel plates for a wide range of aspect ratios and non-dimensional impulse I^*. An analytical solution has been developed, within the constitutive framework of limit analysis, which successfully predicts the location of tear initiation and the critical impulses at mode transitions. Predictions by the theory is shown to be in good agreement with the results from FE and, also, with experimental results. The non-convergence of key local stresses near the plate boundary, due to stress singularities, has been addressed which, subsequently, allowed ductile fracture along the plate boundary to be modelled, within the framework of damage mechanics, using finite elements. The parametric study reveals a number of key features regarding the impulsive response of rectangular plates as follows:

- The impulsive mode II response has been reclassified into three distinct types, depending on whether tearing initiates at the support.
- The central deflection of a rectangular plate deforming in modes I and II(Types $1+2$) decreases with aspect ratio for the same I^*.
- With increasing plate aspect ratio and thickness, a higher non-dimensional impulse I^* is needed to cause non-through-thickness and through-thickness tearing at the support.
- The mode III response is insensitive to aspect ratio γ and plate thickness. For thin plates, the critical impulse for transition to mode III transition is a function of material properties.
- An increase in the blast duration delays the transition between deformation modes for plates of the same dimensions and subjected to the same non-dimensional impulse I^*.

Acknowledgements

The authors are indebted to Dr. Amir Shojaei for the many invaluable discussions and to an anonymous reviewer for his/her helpful comments. This work is supported, in part, by the EPSRC under grant number EP/I028811/1 and, in part, by Lloyd's Register and the Ministry of Defence (UK).

References

[1] Menkes S, Opat H. Broken beams. Exp Mechanics 1973;13:480–6.
[2] Nurick GN, Shave GC. The deformation and tearing of thin square plates subjected to impulsive loads–an experimental study. Int J Impact Eng 1996;18(1):99–116.
[3] Nurick GN, Gelman ME, Marshall NS. Tearing of blast loaded plates with clamped boundary conditions. Int J Impact Eng 1996;18(7–8):803–27.
[4] Olson MD, Nurick GN, Fagnan JR. Deformation and rupture of blast loaded square plates—predictions and experiments. Int J Impact Eng 1993;13(2):279–91.
[5] Rudrapatna NS, Vaziri R, Olson MD. Deformation and failure of blast-loaded square plates. Int J Impact Eng 1999;22(4):449–67.
[6] Ramajeyathilagam K, Vendhan CP. Deformation and rupture of thin rectangular plates subjected to underwater shock. Int J Impact Eng 2004;30(6):699–719.
[7] Xue Z, Hutchinson JW. Preliminary assessment of sandwich plates subject to blast loads. Int J Mech Sci 2003;45(4):687–705.
[8] Xue Z, Hutchinson JW. A comparative study of impulsive resistant metal sandwich plates. Int J Impact Eng 2004;30:1283–305.
[9] Hancock JW, Mackenzie AC. On the mechanisms of ductile fracture in high-strength steels subjected to multi-axial stress states. J Mech Phys 1976;24. 1471–1469.
[10] Johnson GR, Cook WH. A constitutive model and data for metals subjected to large strains, high strain rates and high temperatures. In: Proceedings of 7th international symposium on ballistics. Netherlands: 1983, p. 541.
[11] Jones N. A theoretical study of the dynamic plastic behaviour of beams and plates with finite-deflections. Int J Solids Structures 1971;7(8):1007–29.
[12] Yu TX, Chen FL. The large deflection dynamic plastic response of rectangular plates. Int J Impact Eng 1992;12(4):605–16.
[13] Jones N. Plastic failure of ductile beams loaded dynamically. Trans ASME J Eng Ind 1976;B1:131–6.
[14] Rudrapatna NS, Vaziri R, Olson MD. Deformation and failure of blast-loaded stiffened plates. Int J Impact Eng 2000;24(5):457–74.
[15] Timoshenko SP, Krieger S. Theory of plates and shells. Singapore: McGraw-Hill International Editions; 1959.
[16] Jones N. Structural impact. Cambridge: Cambridge University Press; 1989.
[17] Wen H-M. Deformation and tearing of clamped work-hardening beams subjected to impulsive loading. Int J Impact Eng 1996;18(4):425–33.
[18] Wen HM. Deformation and tearing of clamped circular work-hardening plates under impulsive loading. Int J Press Vessels Piping 1998;75(1):67–73.
[19] Sinclar GB. Stress singularities in classical elasticity-i: removal, interpretation, and analysis. Appl Mechanics Rev 2004;57:251–97.
[20] Sinclar GB. Stress singularities in classical elasticity-ii: asymptotic identification. Appl Mechanics Rev 2004;57:385–439.
[21] Sinclar GB, Beisheim JR, Sezer S. Practical convergence-divergence checks for stresses from fea. In: Proceedings of the 2006 international ANSYS conference. 2006, p. 50.
[22] Shojaei A, Yuan Y, Sinclair G, Tan PJ. On the stress singularity at the fully clamped boundary of finite element problems in structural dynamics, in preparation.
[23] Jones N, Uran TO, Tekin SA. The dynamic plastic behaviour of fully clamped rectangular plates. Int J Solids Structures 1970;6(12):1499–512.
[24] ABAQUS/Explicit, user's manual version 6.10. volume. Hibbitt HD, Karlsson BI, Sorensen I: Hibbit, Karlsson and Sorenson Inc. Pawtucket.